Supporting Information

Embedding the intermetallic Pt_5Ce alloy in mesopores through Pt-C coordination layer interactions as stable electrocatalyst for oxygen reduction reaction

Nannan Jiang, [a,b] *Hao Wang,*[a] *Huihui Jin,*[a], *Xuwei Liu,*[a,b] *and Lunhui Guan*[*,a]

[a] State Key Laboratory of Structural Chemistry, Fujian Key Laboratory of Nanomaterials, and CAS Key Laboratory of Design and Assembly of Functional Nanostructures, Fujian Institute of Research on the Structure of Matter, Chinese Academy of Sciences, Fuzhou, Fujian 350002, China

[b] University of Chinese Academy of Sciences, Beijing, 100049, China

* Corresponding author.
E-mail address: guanlh@fjirsm.ac.cn

Table of Contents

The file includes：

1. Experimental Section

1.1 Chemical.

The chemical reagents used in the experiments included: chloroplatinic acid hexahydrate ($H_2PtCl_6·6H_2O$, 99.9%, Pt:37.5%+), cerium (III) chloride heptahydrate ($CeCl_3·7H_2O$, 99.99%), tetraethoxysilane ($C_8H_{20}O_4Si$, 99%, TEOS), ammonium hydroxide solution (NH_4OH, 25-28%), dopamine hydrochloride ($C_8H_{12}ClNO_2$, 99%+, DA), melamine ($C_3H_6N_6$, 99%) were purchased from Adamas. Ethanol (C_2H_5OH) and hydrochloric acid (HCl, 37 %) were purchased from Sinopharm Chemical Reagent Co. Conductive carbon black Ketjenblack (EC600JD, KB) was bought form Suzhou Yilong Energy Technology Co., Ltd.. Nafion perfluorinated resin ($C_9HF_{17}O_5S$, 5wt.% in mixture of lower aliphatic alcohols and water, contains 45% water), and 2-propanol (C_3H_8O, 99.9%) were bought from Sigma-Aldrich. Perchloric acid ($HClO_4$, 70.0～72.0%) and sodium hydroxide (NaOH, 97.0-100.5%) were purchased from Greagent. Pt/C (20 wt%, 60 wt%) were purchased from Johnson-Matthey. All the chemicals were used without further purification. Deionized water (DI) was used in all experiments.

1.2 Catalyst synthesis.

Preparations of N-KB. At room temperature, 1 g KB and 4 g $C_3H_6N_6$ were mixed with ethanol and ground into a paste. Dried at 60 ^oC. Finally, the powder was calcined

in a N_2 atmosphere at 700 ^oC for 30 min.

Preparations of N-HMCS. Take 70 mL ethanol, 13 mL DI, and 1.8 mL NH_4OH stirred at room temperature for 40 min. Then, slowly added 2.5 mL TEOS. After 2 h, washed procedure with ethanol and DI till the dispersion media became pH neutral. Lyophilized to obtain SiO_2 nanoparticles. Take 80 mL ethanol, 20 mL DI, and added 100 mg of SiO_2 nanoparticles, sonicated for 15 minutes. At 40 ^oC, added 200 mg DA, 1 mL NH_4OH, vigorously stirred for 24 h to allow DA to polymerize on the surface of silica. Washed with ethanol and DI till the dispersion media became pH neutral. Then, lyophilized to obtain reddish-brown SiO_2@PDA precipitate. The 100 mg synthesized SiO_2@PDA was carbonized under an Ar atmosphere at 900 ^oC for 2 h to obtain N, C-SiO_2, followed by the removal of the SiO_2 template agent in a 4 M sodium hydroxide aqueous solution at 80 ^oC for 24 h, then washed and collected N-HMCS by centrifugation method multiple times.

Preparations of E-Pt_5Ce. 0.52 g $H_2PtCl_6 \cdot 6H_2O$, 0.08 g $CeCl_3 \cdot 7H_2O$, and 1.71 g carbon support sonicated in DI for 30 min. Then lyophilized. The mixture was filled into a high-purity graphite rod and installed in an arc furnace. The rapid Joule thermal shock (RJTS) method can achieve instantaneous heating and rapid cooling by the electric field switch. We performed pyrolysis by heat treatment at 80 A for 100 s. With the Joule thermal equipment, we were able to obtain real-time temperature measurements using an infrared temperature detector. We raised the temperature to approximately 1050 °C within 5 s, maintained it for 95 s, and rapidly cooled it to room temperature within 10 s. Then, the obtained materials were treated in a beaker with 2

mol L^{-1} HCl at 60 °C for 1 h. Finally, the E-Pt_5Ce were put in the air at 200 °C for 12 h by mild oxidation removal.

Preparations of L-Pt_5Ce. The synthesis steps and dosage perfectly aligned with the preparation of E-Pt_5Ce, with the only difference being the substitution of the carbon support with N-KB.

1.3 Physical characterization.

Powder X-ray diffraction (XRD) measurements were performed with a MiniFlex 600 X-ray diffractometer (Rigaku) using a Cu kα (λ= 0.154 nm) radiation source with 30 kV and 15 mA. The scan speed was 1° per minute. We calculate the particle mean size by Debye-Scherrer formula (eq 1).

$$D = \frac{K\lambda}{\beta cos\theta} \quad \text{(eq 1)}$$

the average grain size is D, the crystal shape factor K values 0.9, the diffraction angle θ and semi-peak width β, respectively. The results from quantitative inductively coupled plasma-optical emission spectroscopy (ICP-OES) analysis revealed that the molar ratios of Pt to Ce in the samples were nearly identical. Consequently, Pt_5Ce alloys with approximately 9 wt% Pt loading on the N-doped carbon support were synthesized, based on these findings. X-ray absorption spectroscopy (XAS) spectra were acquired at the Shanghai Synchrotron Radiation Facility (SSRF) and analyzed using Athena software. Raman spectra were obtained using the Horiba Jobin Yvon LabRAM ARAMIS system with 633 nm light. Prior to recording the Raman spectra, the system underwent calibration using a Si plate. XPS spectra were measured on ESCALAB 250Xi (ThermoFisher) and calibrated to adventitious C1s peak at 284.8 eV.

Transmission electron microscope (TEM) images were obtained at 200 kV with a Talos-F200X and Tecnai G^2 F20. The high-angle annular dark-field scanning transmission electron microscopy (HAADF-STEM) images were obtained with a Talos-F200X at 200 kV. Energy-dispersive X-ray spectroscopy (EDS) analyses were performed on aberration corrected TEM using Talos-F200X at 200 kV. The inner morphology of the synthesized samples was analyzed using TEM, with high-resolution (HR)-TEM employed for detailed morphology analysis. Over 500 particles were counted across 3 to 5 TEM images to accurately determine the particle size distribution of each sample. The elemental mappings were acquired by EDS characterization. The Special Aberration Corrected Transmission Electron Microscope (AC-TEM) image was obtained by JEM-ARM300F. The specific surface areas of carbon supports were measured using the Brunauer-Emmett-Teller (BET) surface area analyzer (Autosorb IQ). The contact angle tests were acquired by LSA100 contact angle tester and analyzed using SurfaceMeter.

1.4 Electrochemical measurements.

In order to assess the oxygen reduction reaction (ORR) performance, a typical three-electrode configuration with rotating disk electrode (RDE) setup was applied. A Pt foil was applied as the counter electrode, and a commercial Ag/AgCl was used as the reference electrode. 5 mg of the catalysts were added to 1 mL of solution consisted of Nafion solution (5 wt%) and 2-propanol. The Pt loading of synthesized samples and the commercial Pt/C (20 wt %) on the glassy carbon electrode (0.196 cm^2) was kept at

8.9 μg_{Pt} cm^{-2}, followed by drying at room temperature. All electrochemical measurements were performed in 0.1 M $HClO_4$ at 25 °C. Cyclic voltammetry (CV) measurement was conducted in O_2-saturated 0.1 M $HClO_4$ for at least 60 cycles. Secondly, the linear sweep voltammetry (LSV) curves were performed to evaluate the electrochemical performance in O_2-saturated 0.1M $HClO_4$ at 10 mV s^{-1} with 1600 rpm. The curves were calibrated with the background subtraction and solution resistance. According to the Koutecky-Levich equation (eq 2), the kinetic currents could be calculated. The mass activity (MA) could be calculated according to eq 3. And as for eq 4, the specific activity (SA) could be calculated.

$$\frac{1}{i} = \frac{1}{i_L} + \frac{1}{i_K} \quad \text{(eq 2)}$$

where i is the measured current and i_L is the diffusion-limited current.

$$MA = \frac{i_K}{m_{Pt}} \quad \text{(eq 3)}$$

where m_{Pt} is the Pt loading of the catalyst used in the working electrode.

$$SA = \frac{i_K}{ECSA} \quad \text{(eq 4)}$$

where ECSA is the electrochemical surface area of the catalyst, which can be estimated by a hydrogen underpotential deposition (Hupd) method. Besides, to assess the ECSA, the Hupd method (assuming factor = 210 μC cm^{-2}) was applied. The Hupd method was conducted in 0.1 M $HClO_4$ saturated with N_2 (100 mV s^{-1}). In the potential range of around 0.011 V and 0.406 V after the deduction of the capacitive current, which contain the Hupd adsorption/desorption peak, and the charge (Q_H) was obtained. The baseline used for integration of the Q_H belonging to the Hupd

adsorption/desorption peak was the current value at around 0.406 V. According to the eq 5, the ECSA obtained via the Hupd method was estimated.

$$ECSA = \frac{Q_H}{q_H \cdot m_{Pt}} \text{ (eq 5)}$$

where Q_H represents the total charge associated with the hydrogen desorption peak after double-layer correction, q_H represents the charge required for a single adsorbed hydrogen molecule on a unit area of Pt surface, which has a value of 210 μC cm_{Pt}^{-2}, m_{Pt} is the Pt loading of the as-prepared catalyst used in the working electrode. The average charge of the H adsorption and desorption peak was applied to estimate the ECSA (denoted as $\overline{Hs}$) for comparison. At last, the stability of the catalysts was assessed by using an accelerated durability test (ADT) at 0.6-1.0 V (vs RHE, 100 mV s^{-1}) in the O_2 atmosphere.

1.5 PEMFC measurement.

To prepare the cathode catalyst ink, the catalysts were ultrasonically dispersed in 1:1 n-propanol/water solution with 5wt% Nafion solution for 30–60 min. The catalyst-coated-membrane (CCM) was prepared by using ultrasonic spray to direct spray the ink on the Nafion membrane with an active area of 25 cm^2. The synthesized samples and commercial Pt/C (20 wt%) were both utilized as cathode catalysts, while 60 wt% commercial Pt/C was employed as the anode catalyst. The Pt loading for both the cathode and anode was maintained at 0.1 mg_{Pt} cm^{-2}. The fabricated CCM was dried to completely evaporate the solvents. A gas diffusion layer (GDL) including a microporous layer was used (SGL Carbon Sigracet 22 BB) with a thickness of 0.215 ±

0.02 mm thickness. Two GDLs, two gaskets, and the prepared CCM were pressed to obtain the membrane electrode assembly (MEA).

The performance of the MEA was evaluated using the Hephas 850e. The test condition was set at 80 °C, 100% RH, 1 bar H_2/O_2 or H_2/Air with 2/5 L min^{-1}. The ADT was performed by square wave cycling. The durability test conditions refer to the ADT protocol of US Department of Energy (DOE). The ADT was performed by square wave cycling, with each cycle holding the MEA at a voltage of 0.6 V for 3 s and then 0.95 V for 3 s, at 80 °C, 100% RH, atmospheric pressure H_2/N_2 with 0.2/0.075 L min^{-1}. The dry proton accessibility (DPA) was measured by comparing the calculated values of ECSA at 20% RH and 100% RH under the H_2/N_2 atmosphere.

1.6 Density functional theory (DFT) calculations.

The density functional theory (DFT) calculations in this study were executed employing the Vienna Ab Initio Simulation Package (VASP). Evaluation of the exchange-correlation energy was performed using the Generalized Gradient Approximation (GGA) coupled with the Perdew-Burke-Ernzerhof (PBE) functional. The electron-ion interactions were described through the Projector Augmented Wave (PAW) method. The plane wave expansion energy cutoff was established at 500 eV. Convergence criteria were set at 10^{-5} eV for energy and 0.02 eV $Å^{-1}$ for force. In slab model computations, a 15 Å vacuum spacing was introduced to mitigate interactions between periodic images. Furthermore, for these models, dipolar correction was applied with the symmetrization disabled. The K-POINT setting was adjusted to 2 x 2 x 1. Spin polarization was taken into account. The methodology for assessing Oxygen Reduction

Reaction (ORR) performance on slab models was based on the typical adsorbate evolution mechanism proposed by Nørskov et al. To reduce total energy deviations in slab simulations, dipole corrections were employed. The Gibbs free energy variation for each step was computed using the equation: $\Delta G = \Delta E + \Delta ZPE - T\Delta S$. Here, ΔE denotes the total energy difference between reactant and product molecules adsorbed on the catalyst surface, ΔZPE represents the zero-point energy correction, T is the temperature (298.15 K), and ΔS signifies the change in vibrational entropy.

Table S1. The bulk elemental compositions of samples determined by XPS and EDS.

Sample	Determined by XPS		Determined by EDS	
	C / at%	N / at%	C / at%	N / at%
Pt/C	83.03	-	95.12	-
N-HMCS	98.22	1.78	97.65	2.35
N-KB	97.07	2.93	96.12	3.88

Table S2. The bulk elemental compositions of samples determined by ICP and XPS.

Sample	Determined by ICP			Determined by XPS			
	Pt / wt%	Ce / wt%	Pt/Ce ratio	N / at%	Pt / at%	Ce / at%	Pt/Ce ratio
Pt/C	19.68	-	-	-	-	-	-
E-Pt_5Ce	8.72	1.25	6.98	1.92	81.43	16.65	4.89
L-Pt_5Ce	8.99	1.27	7.01	2.34	80.47	17.19	4.68

Table S3. The best-fitted EXAFS results of E-Pt_5Ce and L-Pt_5Ce.

Sample	Path	CN [a]	R (Å) [b]	σ^2 ($Å^{-2}$) [c]	ΔE_0 (eV) [d]	R factor [e]
Pt foil	Pt-Pt	12 [f]	2.761±0.002	0.0041±0.0003	7.96±0.35	0.0015
PtO_2	Pt-O_1	5.8±0.2	2.015±0.005	0.0021±0.0005	10.29±0.30	0.0132
	Pt-Pt_1	5.6±0.5	3.104±0.004	0.0024±0.0004		
	Pt-Pt_2	7.2±0.4	3.754±0.004	0.0196±0.0086		
	Pt-O_2	5.5±0.2	3.669±0.010	0.0037±0.0012		
L-Pt_5Ce	Pt-C	0.5±0.1	2.007±0.014	0.0105±0.0059	3.24±0.28	0.0121
	Pt-Pt	8.0±0.2	2.694±0.003	0.0067±0.0003		
	Pt-Ce	0.8±0.2	2.834±0.004	0.0118±0.0034		
E-Pt_5Ce	Pt-C	1.8±0.3	2.037±0.024	0.0193±0.0043	3.26±0.35	0.0167
	Pt-Pt	8.6±0.3	2.698±0.003	0.0053±0.0002		
	Pt-Ce	0.9±0.1	2.840±0.004	0.0011±0.0004		

[a] *CN*: coordination numbers; [b] *R*: bond distance; [c]σ^2: Debye-Waller factors; [d]ΔE_0: the inner potential correction. [e] *R* factor: goodness of fit. [f] the parameter was fixed during fitting process. The obtained XAFS data was processed in Athena (version 0.9.26) for background, pre-edge line and post-edge line calibrations. Then Fourier transformed fitting was carried out in Artemis (version 0.9.26). S_0^2 was fixed as 0.80.

The k-range of 3 – 12 $Å^{-1}$ and R range of 1 – 3 Å were used for the fitting of L-Pt_5Ce, E-Pt_5Ce and Pt foil.

The k-range of 3 – 12 $Å^{-1}$ and R range of 1 – 4 Å were used for the fitting of PtO_2.

Table S4. The electrochemical tests of Pt-RE reported recent years.

Sample	Catalytic activities at 0.9 V (*vs*. RHE)		Improvement factor (a)	Improvement factor (b)	After ADT		Reference
	MA ($A\ mg^{-1}_{Pt}$)	SA ($mA\ cm^{-2}_{Pt}$)			SA ($mA\ cm^{-2}_{Pt}$)	Improvement factor (c)	
Pt_2Gd	1.51	-	5.0	-	(MA) -40%	-	*Natl Sci Rev,* **2023**, 162, 10[1]
Pt_5Ce	0.69	1.05	2.2	2.6	-	-	*Chem. Mater.* **2022**, 34, 10789[2]
A-Pt-Gd(5/1)	0.35	0.50	-	-	-	-	J.*Phys. Chem. C.* **2020**, 124, 26925[3]
Pt_5Ce(3.5nm)	~ 0.70	1.16	1.4	1.5			
Pt_5Ce(5.7nm)	~ 0.95	2.29	1.9	3.1	-	-	*J. Am. Chem. Soc.* **2020**, 142, 953[4]
Pt_5Ce(8.8nm)	~ 0.80	3.95	1.6	5.3			
Pt_xPr/C	0.70	1.96	1.7	-	-	-	*ACS Appl. Mater. Interfaces.* **2019**, 11, 5129[5]
Pt_xGd(8nm)	3.60	-	3.6	-	-	-32.5% (10k)	*J. Catal.* **2015**, 328, 297[6]
Pt_5Gd(8nm)	~3.30	10.5	13.2	5.2	9.1 (10k)	4.7	*Science* **2016,** 352, 73[7]
Pt_5Ce	-	7.4	-	3.5	6.6 (10k)	3.4	
E-Pt_5Ce	**2.86**	**2.03**	**15**	**4.7**	**1.88 (30k)**	**6.7**	**This work**
L-Pt_5Ce	**1.92**	**1.67**	**10.1**	**4.1**	**1.49 (30k)**	**5.3**	**This work**

(a) Improvement factor was determined by MA (sample)/ MA (Pt) in the literature.

(b) Improvement factor was determined by SA (sample)/ SA (Pt) in the literature.

(c) Improvement factor was determined by after ADT SA (sample)/ SA (Pt) in the literature.

Table S5. High-frequency resistance (HFR) values of the MEA before ADT at various current densities in H_2-O_2 fuel cell

Current density / mA cm^{-2}	HFR for E-Pt_5Ce / mΩ cm^2	HFR for L-Pt_5Ce / mΩ cm^2	HFR for Pt/C / mΩ cm^2
40	117	103	83
60	117.25	103	82.5
80	116.5	102.75	82.75
100	116.5	102.75	82.75
120	116	102	82.75
160	115.5	102.75	83.25
200	115.75	102.25	83.25
300	116	102.25	83.75
400	115.75	102.25	83.75
600	111	99.75	82.5
800	106.75	98.75	79.25
1000	101	89	77.75
1200	95.5	85.5	75
1400	90.5	80.75	72.75
1600	87	77	70.5
1800	84.25	74	69
2000	82	72	66.5

Table S6. The PEMFC performance of Pt-based alloy catalysts reported recent years.

Sample	Current density ($A\ cm^{-2}$)	Peak power density ($W\ cm^{-2}$)	MA ($A\ mg^{-1}_{Pt}$)	After 30k cycles		Reference
				Peak power density decayed (%)	MA decayed (%)	
Pt Fe/Fe-N-C (H_2/O_2 1.5 bar)	2.9 (0.6 V)	2.3 (4.2 $A\ cm^{-2}$)	-	-	-	*Adv. Mater.* **2023**, e2300624[8]
L_{10}-PtZn/Pt-C (H_2/O_2 1 bar)	0.55 (0.8 V)	2.0 (4.5 $A\ cm^{-2}$)	0.52	10	16.6	*J. Catal.* **2023**, 45, 17[9]
PtFe-FeNC (H_2/O_2 1 bar)	-	1.08	1.75	12.5	-	*J. Am. Chem. Soc.* **2023**[10]
Pt_3Co/FeN_4 (H_2/Air 1.5bar)	0.35 (0.8 V)	0.82 (1.2 $A\ cm^{-2}$)	0.72	-	38	*Energy Environ. Sci.* **2021**, 14, 4948[11]
Zn-PtNi/C (H_2/O_2 1.5 bar)	~1.6 (0.6 V)	1.3	~0.2	~41 (10k)	-	*Adv. Funct. Mater.* **2022**, 33, 2212442[12]
L_{10} -Pt_2CuGa/C (H_2/O_2 1.5 bar)	~ 0.67 (0.8 V)	2.6 (6.5 $A\ cm^{-2}$)	0.57	15	36	*Angew. Chem. Int. Ed.* **2023**, 62[13]
Co_8Zn_7-Pt (H_2/O_2 1.5 bar)	~0.5 (0.8 V)	1.5	0.75	19	29	*Adv. Energy Mater.* **2022**, 12, 2201600[14]
PtCe/NC (H_2/O_2 1.5 bar)	~0.4 (0.6 V)	0.61	~0.12	31.6	-	*Chem. Asian J.* **2023**, 18, e202300137[15]
E-Pt_5Ce (H_2/O_2 1.5bar)	**0.57 (0.8 V) 0.08 (0.9 V)**	**1.42 (2.0 $A\ cm^{-2}$)**	**0.83**	**4.2**	**14**	**This work**

Table S7. Comparison of of DPA values of Pt_5Ce@C and Commercial Pt/C.

Sample	ECSA (100 RH%) / (m^2 g_{Pt}^{-1})	ECSA (20 RH%) / (m^2 g_{Pt}^{-1})	DPA / %
Pt/C	28.1	23.6	84
E-Pt_5Ce	63.7	27.4	42
L-Pt_5Ce	46.5	28.8	62

Table S8. Comparison of EPSA values of Pt_5Ce@C and Commercial Pt/C.

Sample	Cathode loading / ($mg_{Pt}\ cm^{-2}$)	ECSA (100 RH%) / ($cm^2\ g_{Pt}^{-1}$)	EPSA / ($cm_{Pt}^2\ cm_{MEA}^{-2}$)
Pt/C	0.1	28.1	28.1
E-Pt_5Ce	0.1	63.7	63.7
L-Pt_5Ce	0.1	46.5	46.5

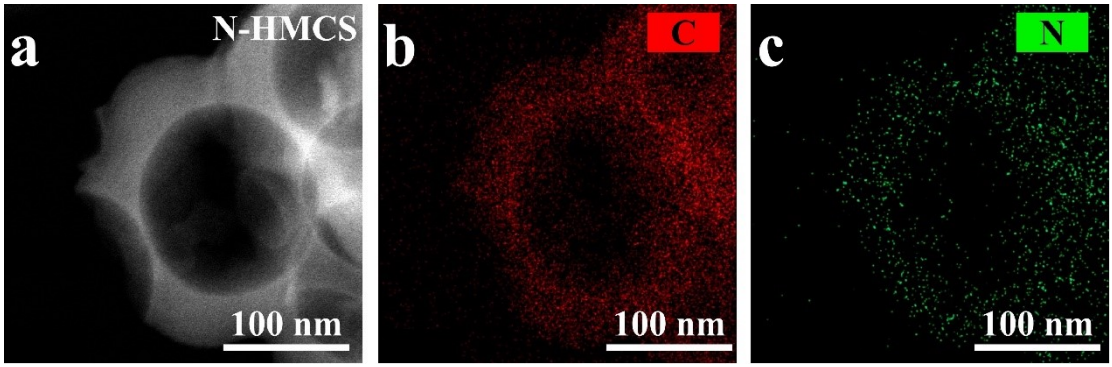

Figure S1. (a) HAADF-STEM image of N-HMCS. EDS mappings of (b) C. (c) N.

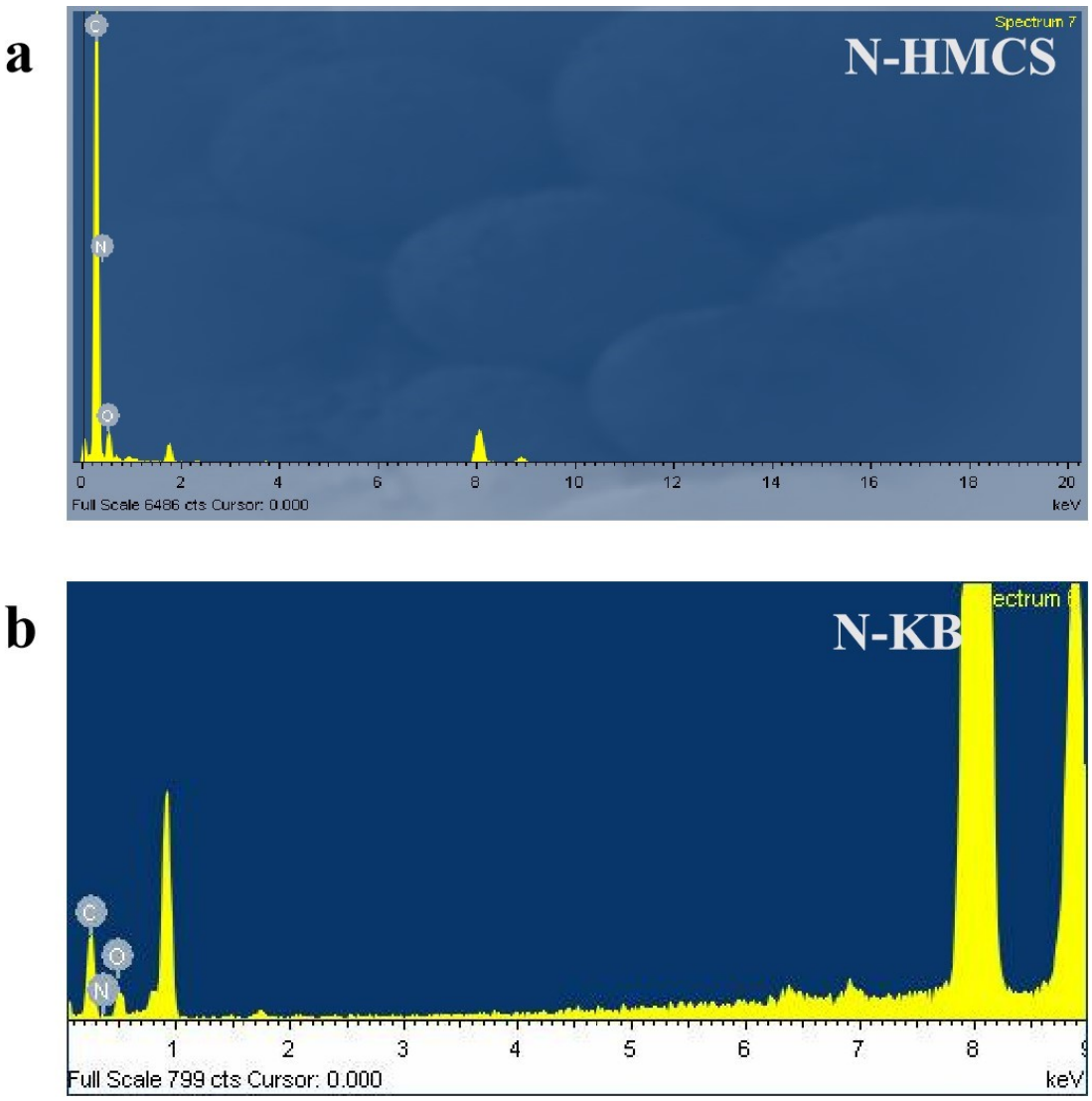

Figure S2. The EDS point analysis results of (a) N-HMCS. (b) N-KB.

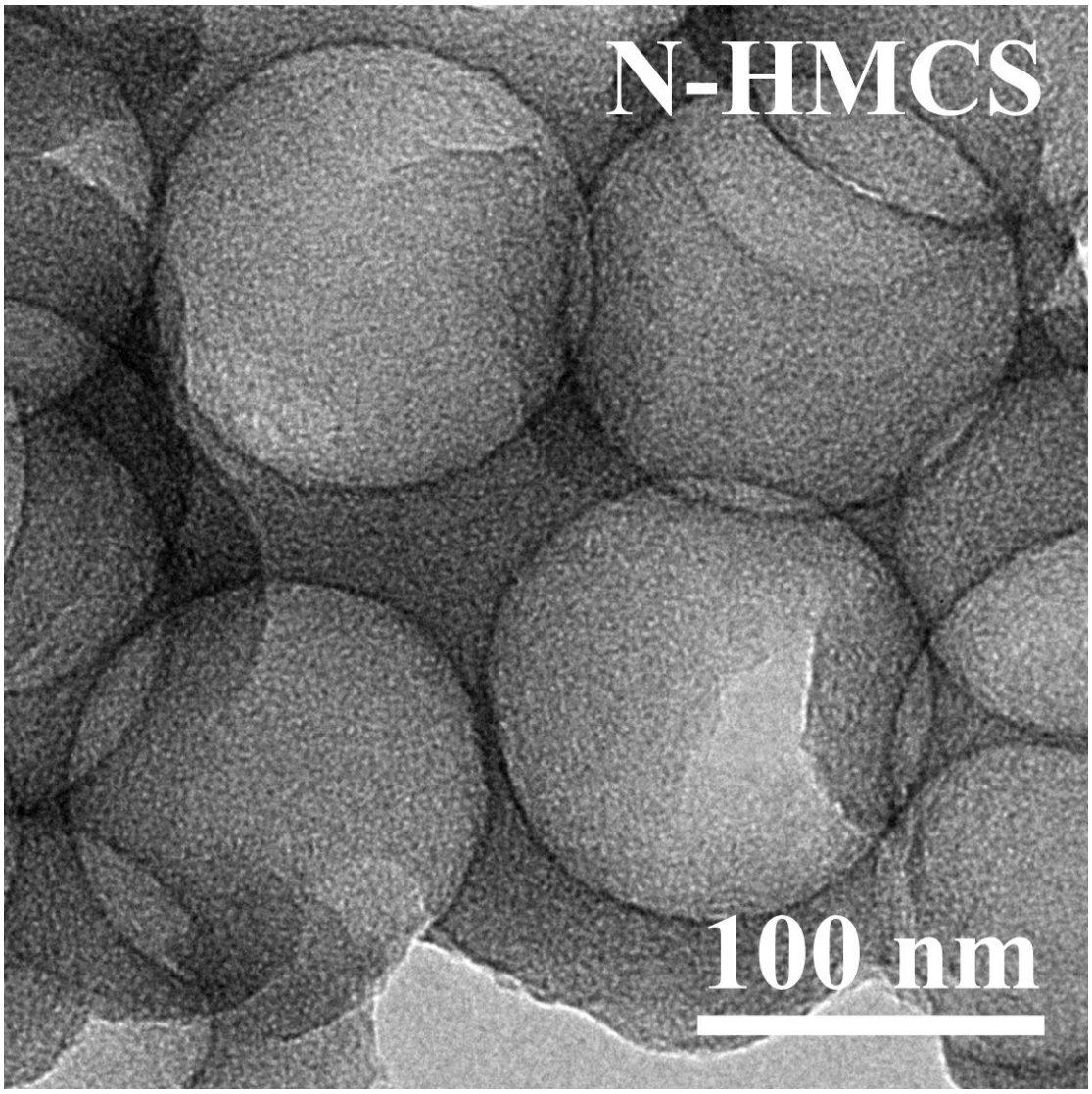

Figure S3. TEM image of N-HMCS.

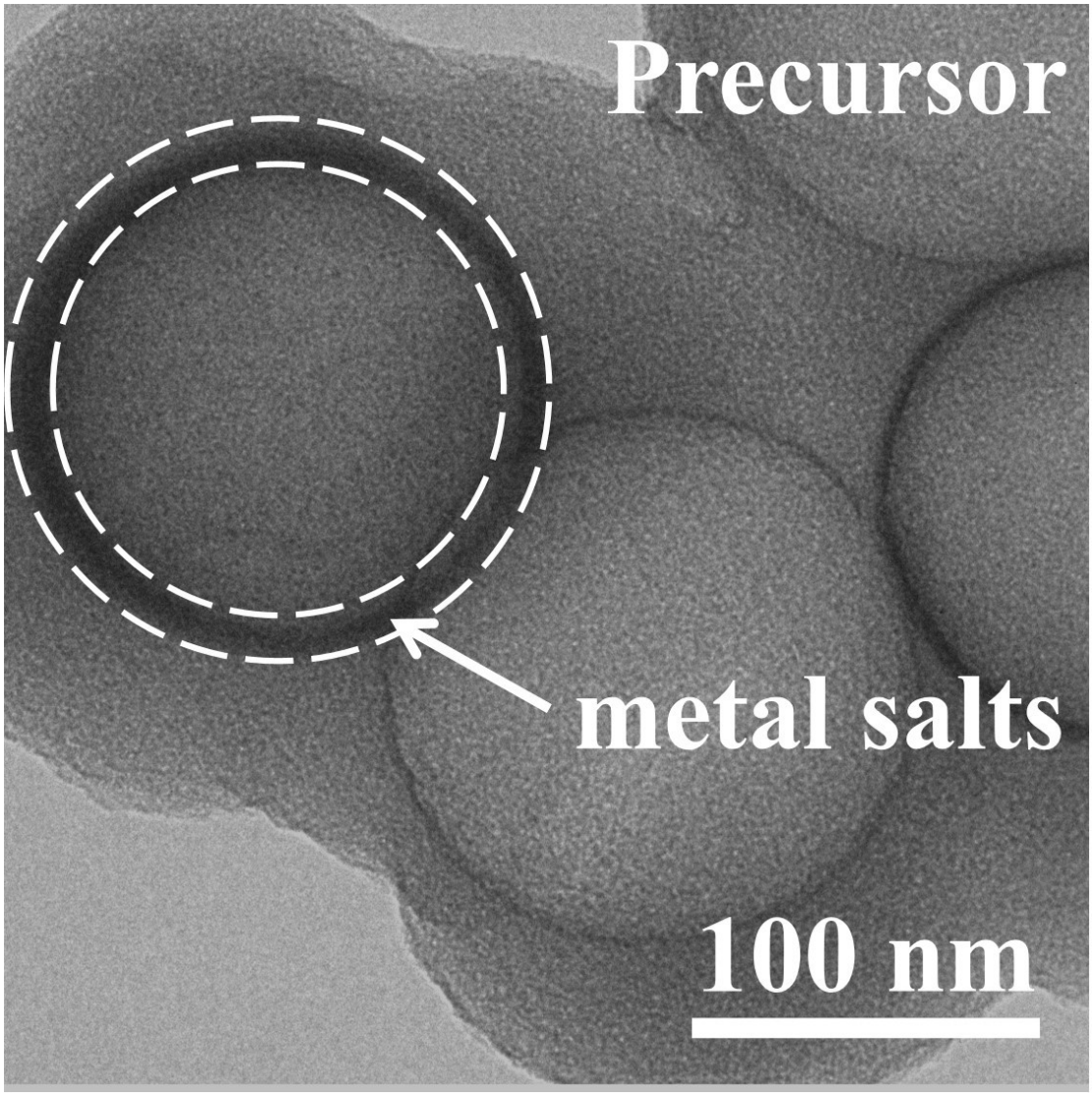

Figure S4. TEM image of precursor. The part indicated by the arrow represents the metal salts aggregated on the shell of the N-HMCS, making it easy to obtain embedded catalysts.

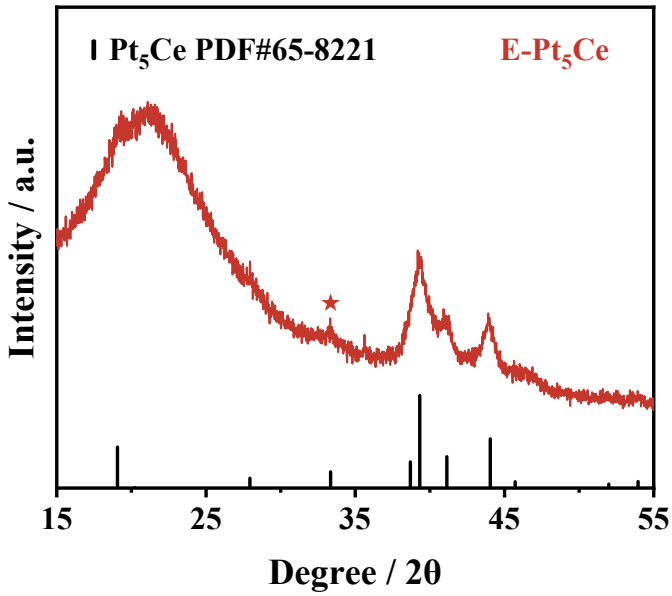

Figure S5. The XRD pattern of E-Pt_5Ce. The corresponding superlattice peak of Pt_5Ce is at 33.5 °, represented by the solid pentagonal center.

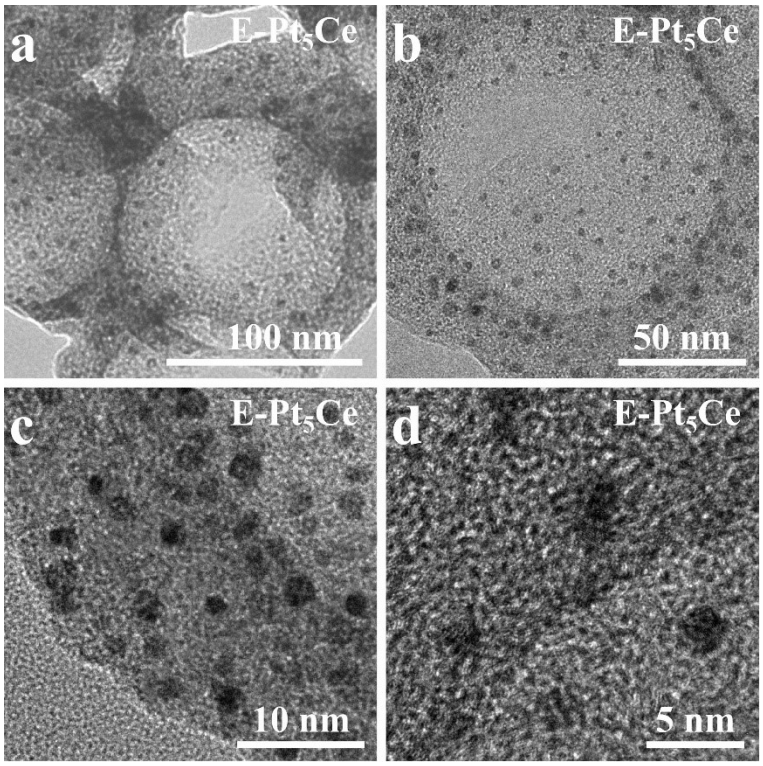

Figure S6. TEM images of E-Pt_5Ce at various magnifications.

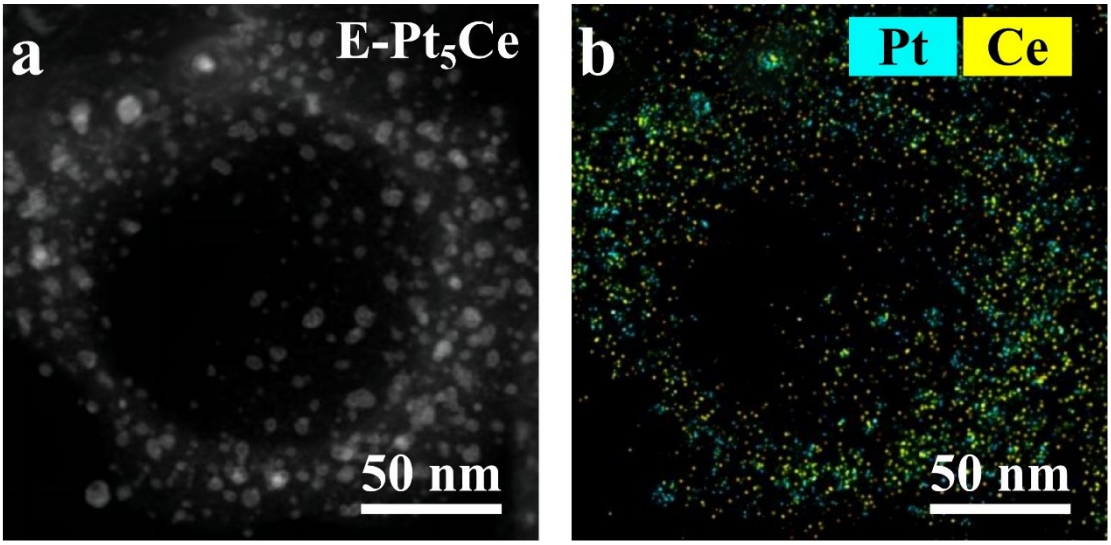

Figure S7. (a) HAADF-STEM image of L-Pt5Ce. (c) EDS mapping of L-Pt5Ce.

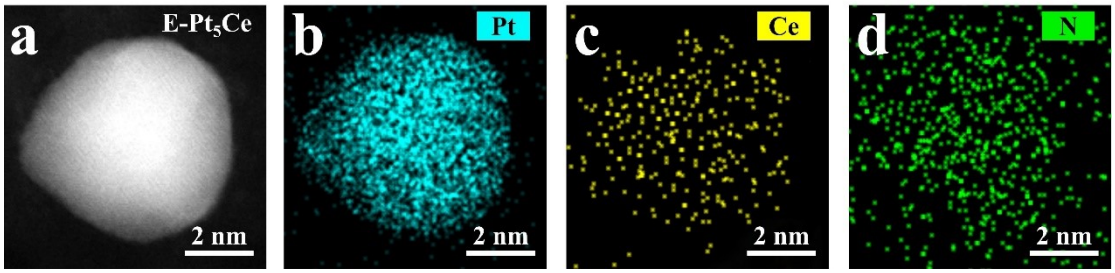

Figure S8. (a) HAADF-STEM image of E-Pt_5Ce. EDS mappings of (b) Pt. (c) Ce. (d) N.

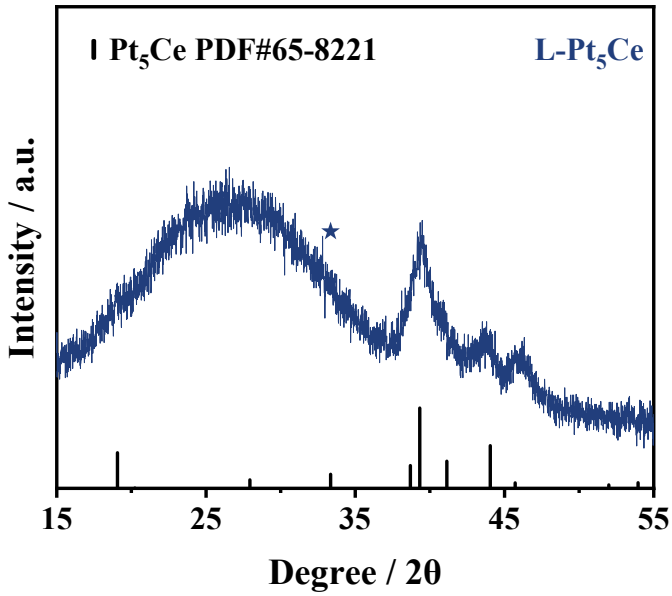

Figure S9. The XRD pattern of L-Pt_5Ce. The corresponding superlattice peak of Pt_5Ce is at 33.5 °, represented by the solid pentagonal center.

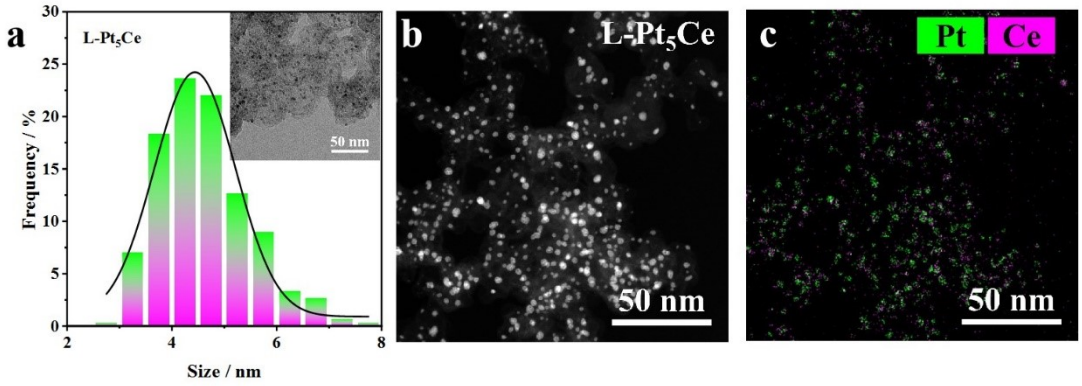

Figure S10. (a) The particle size distribution and TEM image (inset) of L-Pt_5Ce. (b) HAADF-STEM image of L-Pt_5Ce. (c) EDS mappingof L-Pt_5Ce.

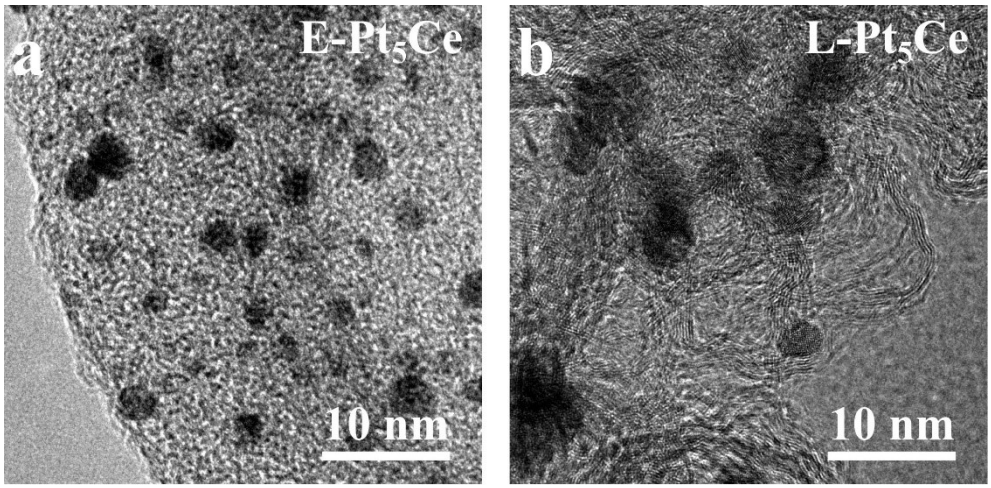

Figure S11. TEM images of (a) E-Pt_5Ce, (b) L-Pt_5Ce.

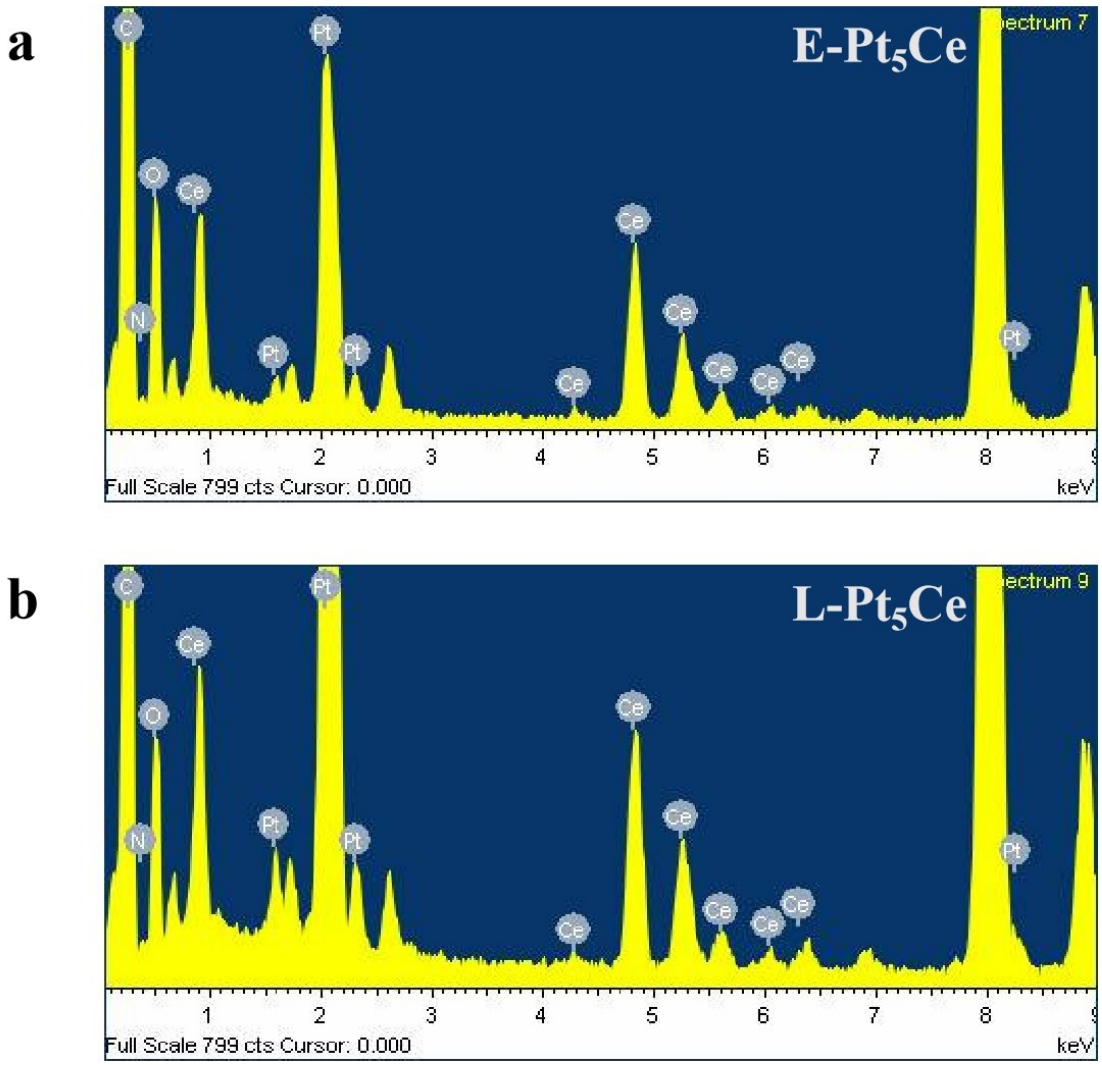

Figure S12. The EDS point analysis results of (a) E-Pt_5Ce. (b) L-Pt_5Ce.

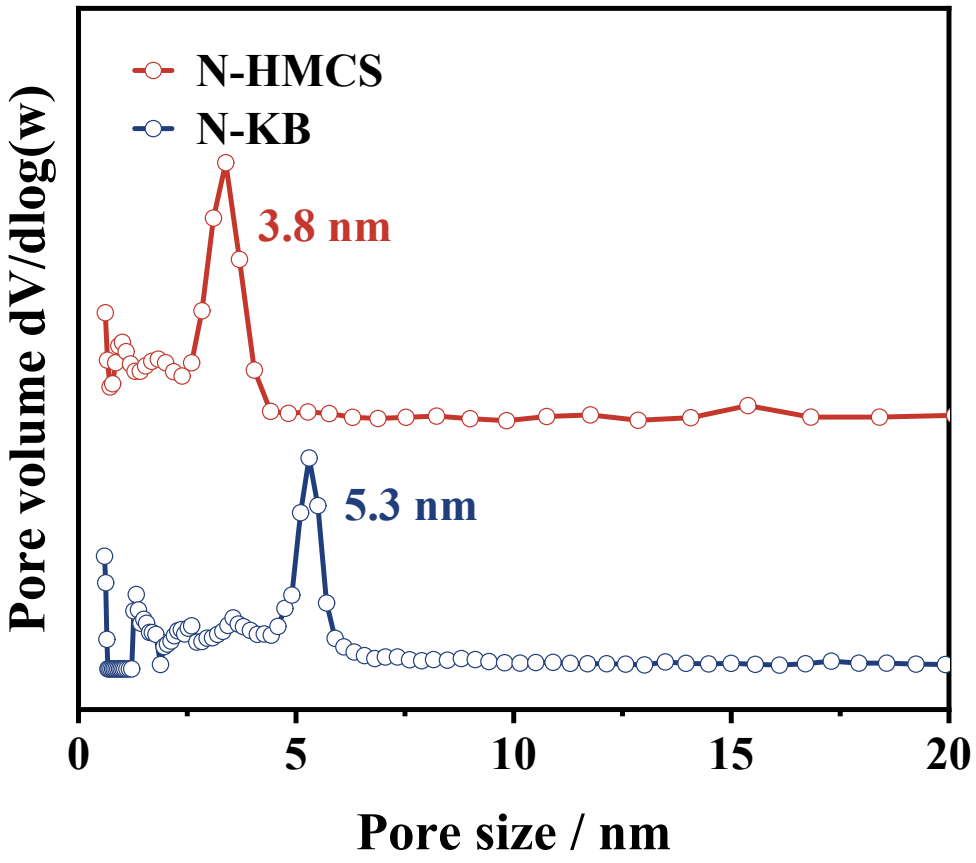

Figure S13. Pore width distributions of carbon supports.

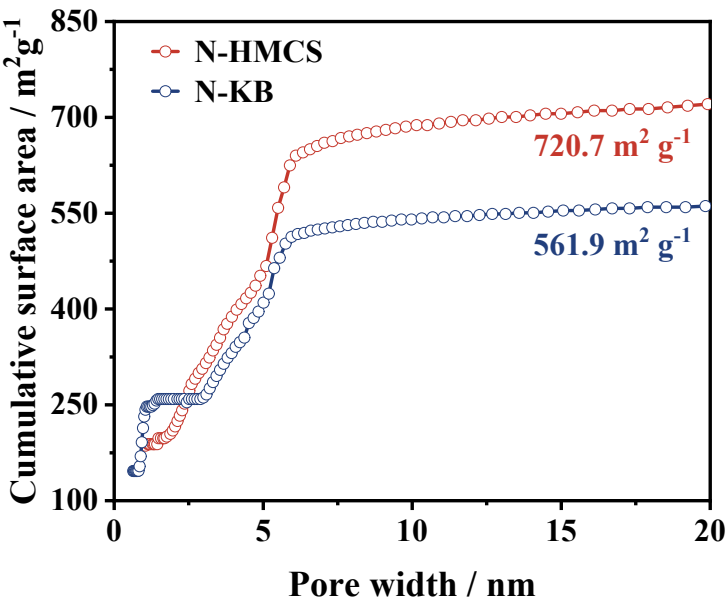

Figure S14. The Brunauer−Emmett−Teller (BET) surface area curves of carbon supports.

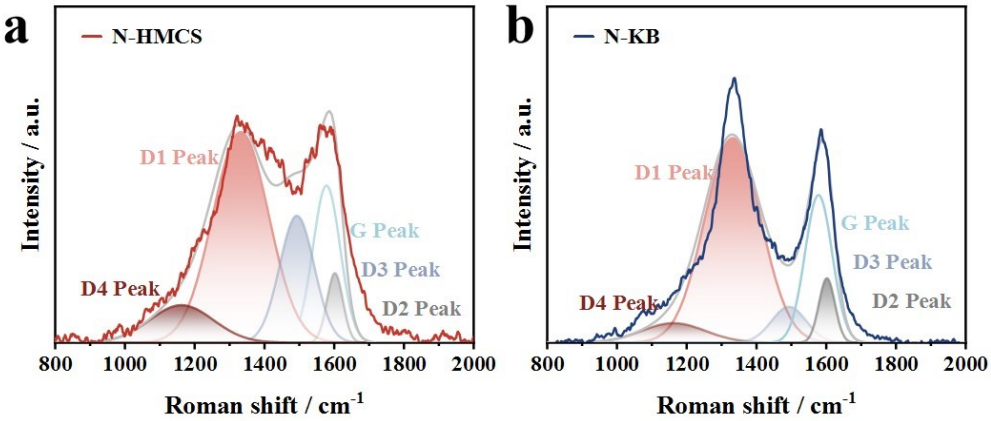

Figure S15. Raman spectra of (a) N-HMCS. (b) N-KB.

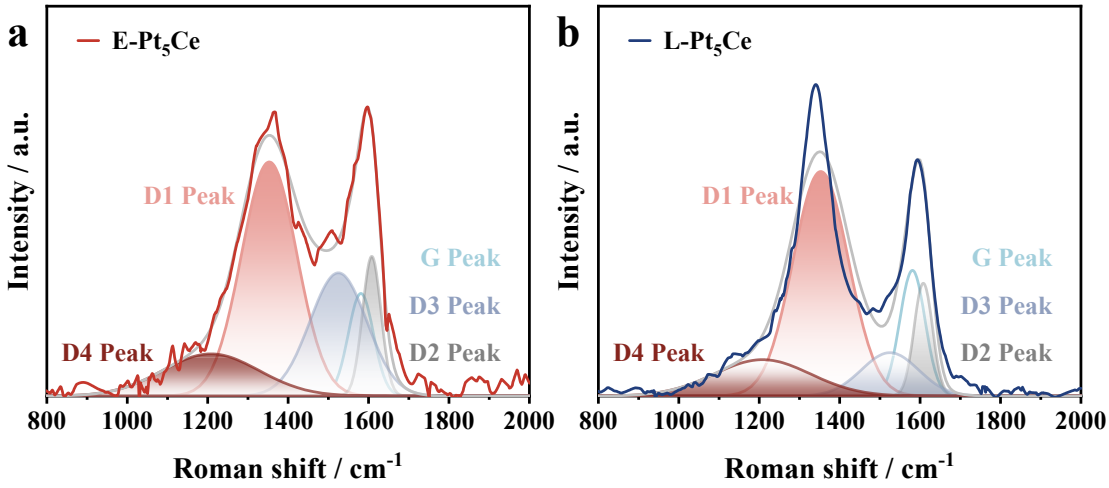

Figure S16. Raman spectra of (a) E-Pt_5Ce. (b) L-Pt_5Ce.

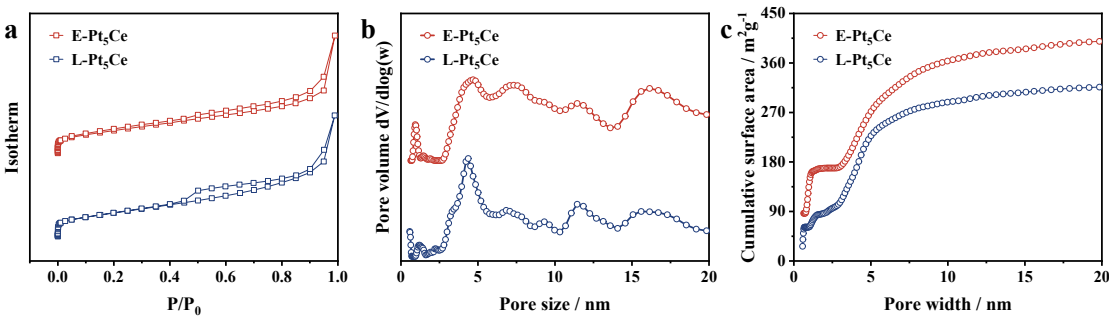

Figure S17. (a) N_2 adsorption−desorption isotherm curves. (b) Pore width distributions curves. (c) The Brunauer−Emmett−Teller (BET) surface area curves of E-Pt_5Ce and L-Pt_5Ce.

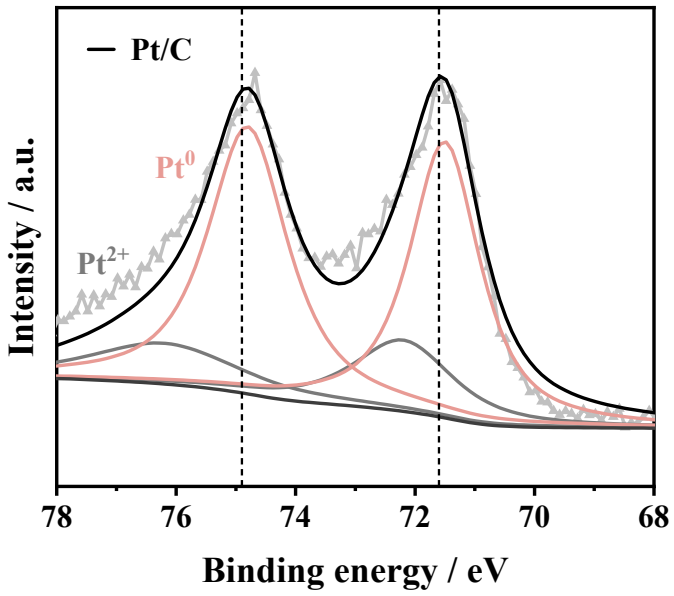

Figure S18. The XPS Pt 4f spectra of commercial Pt/C.

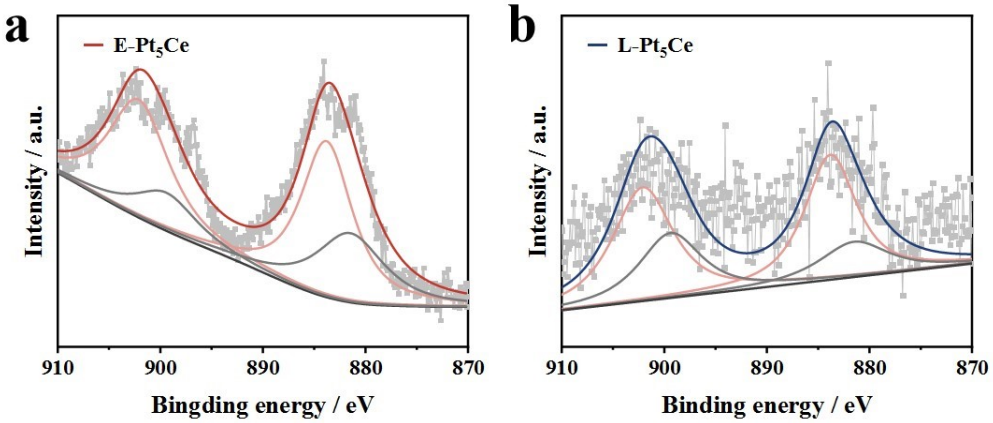

Figure S19. The XPS Ce 3d spectra of (a) E-Pt_5Ce. (b) L-Pt_5Ce.

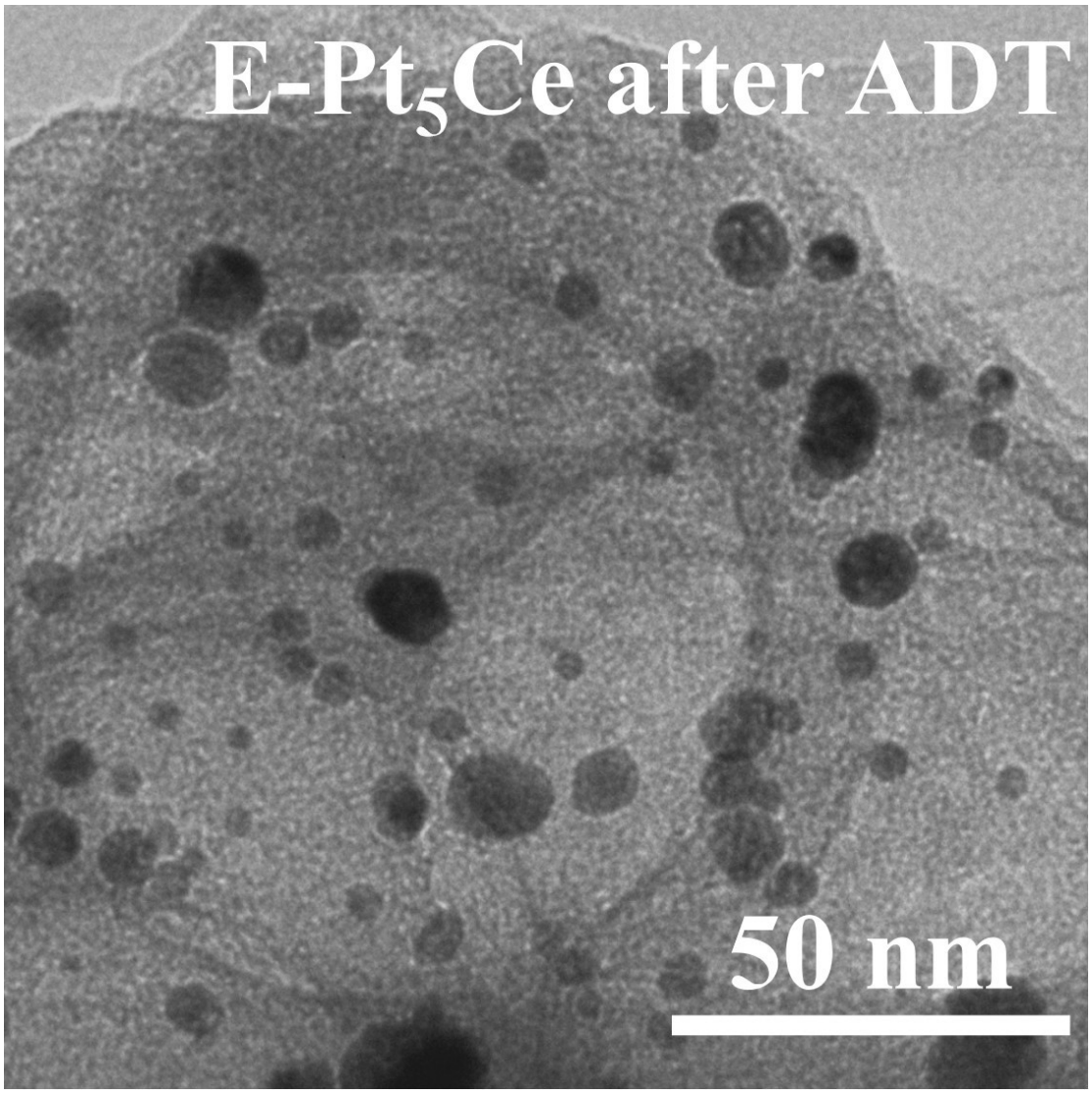

Figure S20. TEM image of E-Pt_5Ce after ADT.

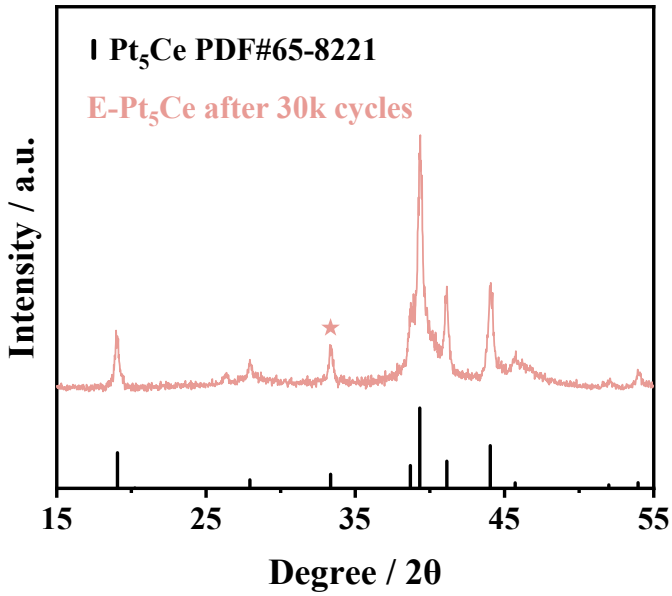

Figure S21. The XRD pattern of E-Pt_5Ce after 30k cycles. The corresponding superlattice peak of Pt_5Ce is at 33.5 °, represented by the solid pentagonal center.

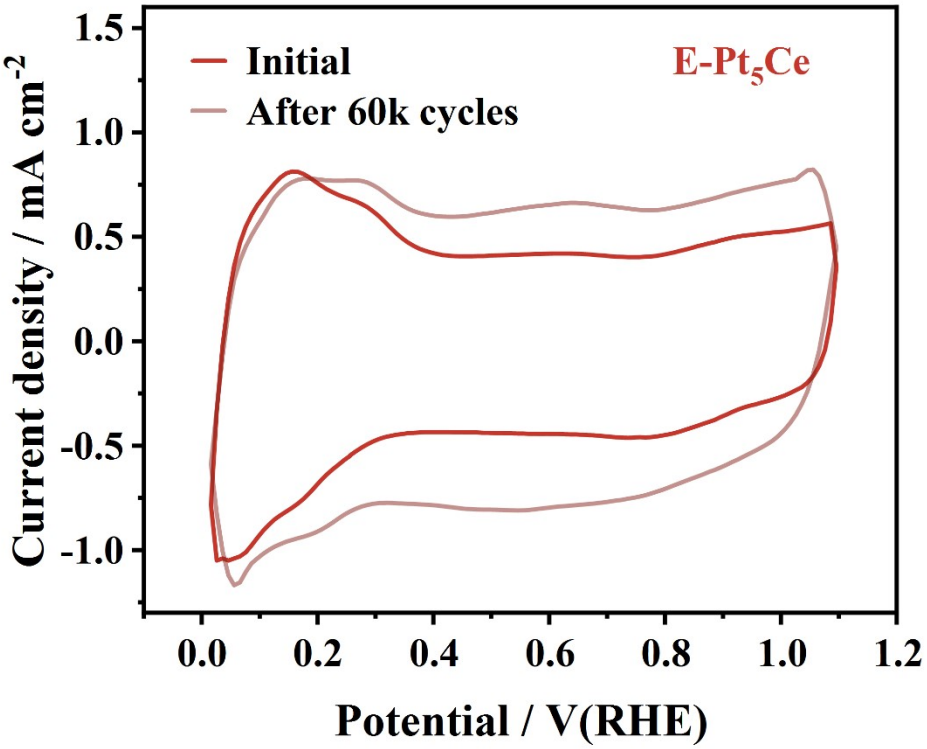

Figure S22. CV curves of initial E-Pt_5Ce and after 60k cycles obtained in N_2-saturated 0.1 M $HClO_4$.

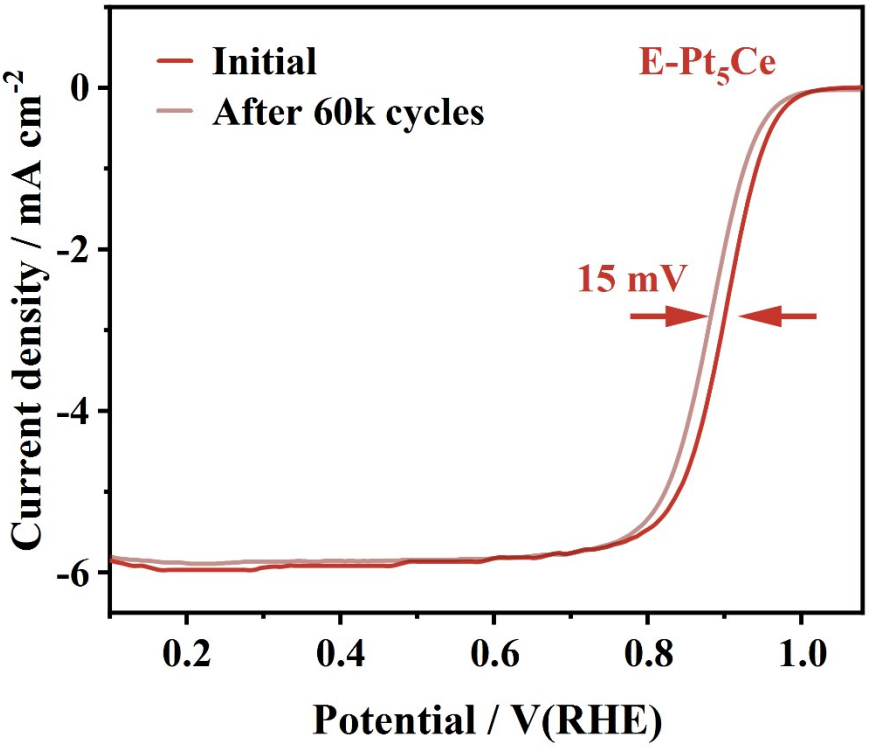

Figure S23. LSV curves of E-Pt_5Ce obtained at 1600 rpm in 0.1 M HClO4.

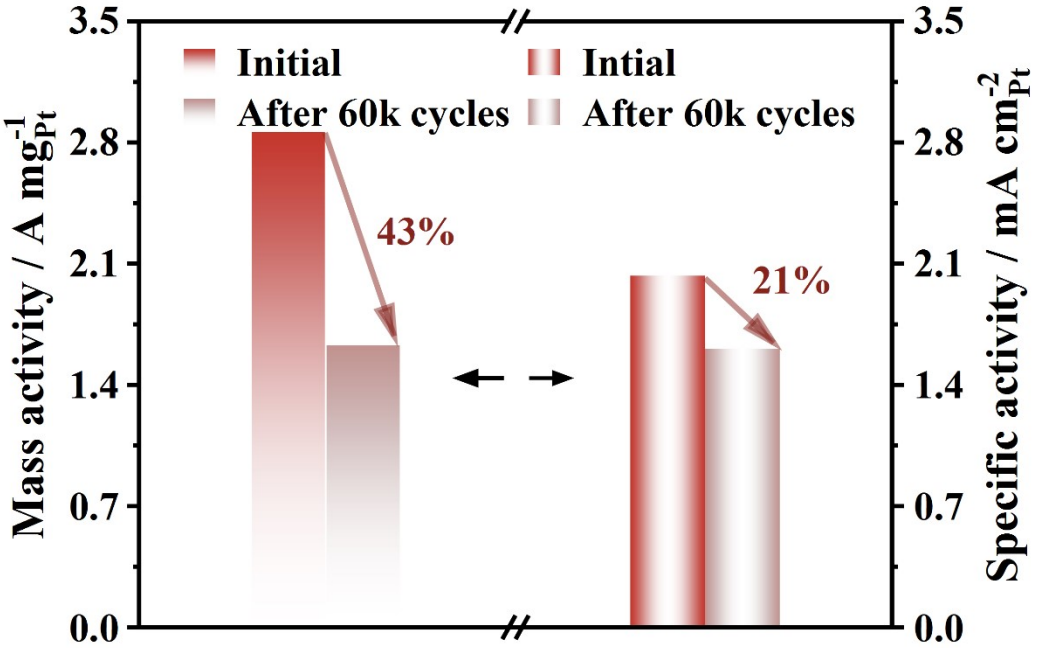

Figure S24. MA and SA values obtained at 0.9 V before and after ADT.

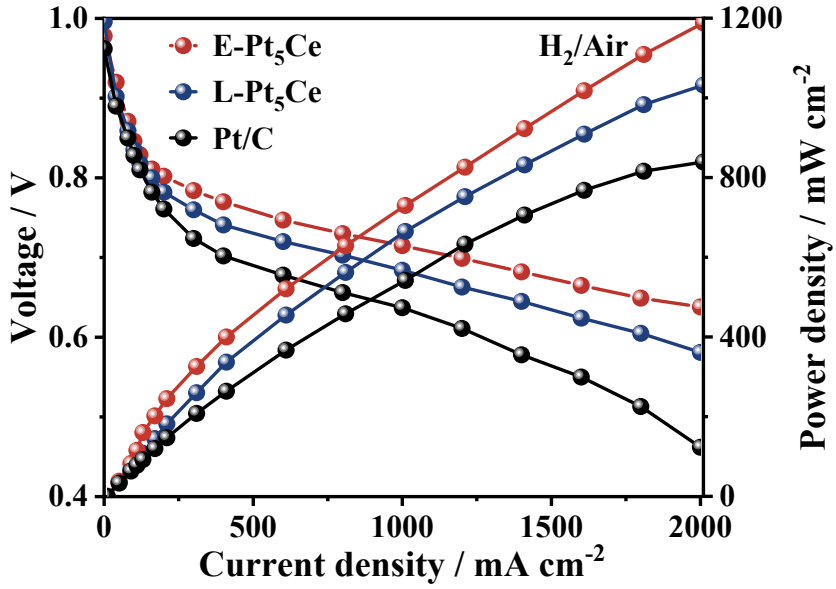

Figure S25. H_2/O_2 polarization and power density curves at 80 °C and 100% RH of E-Pt_5Ce, L-Pt_5Ce and Pt/C.

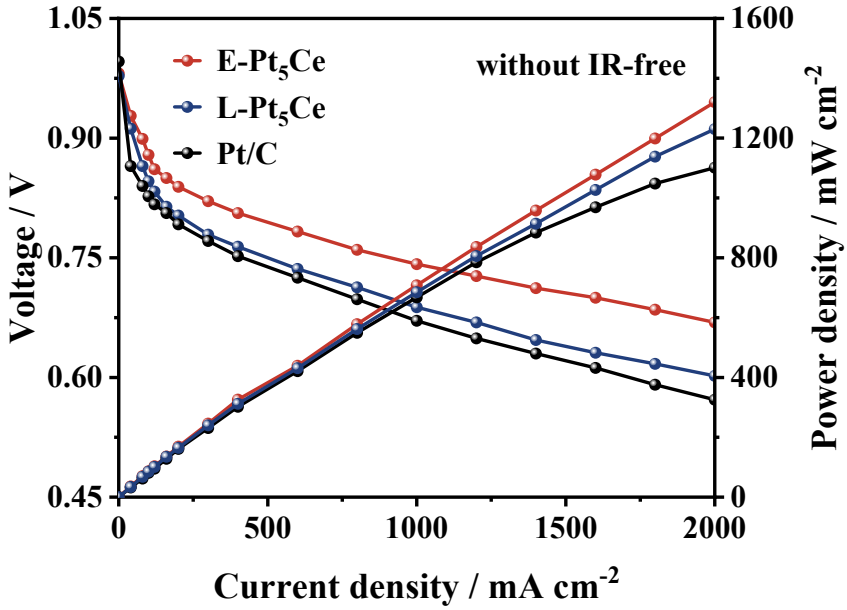

Figure S26. H_2/O_2 polarization and power density curves at 80 °C and 100% RH of E-Pt_5Ce, L-Pt_5Ce and Pt/C in PEMFC without IR-free.

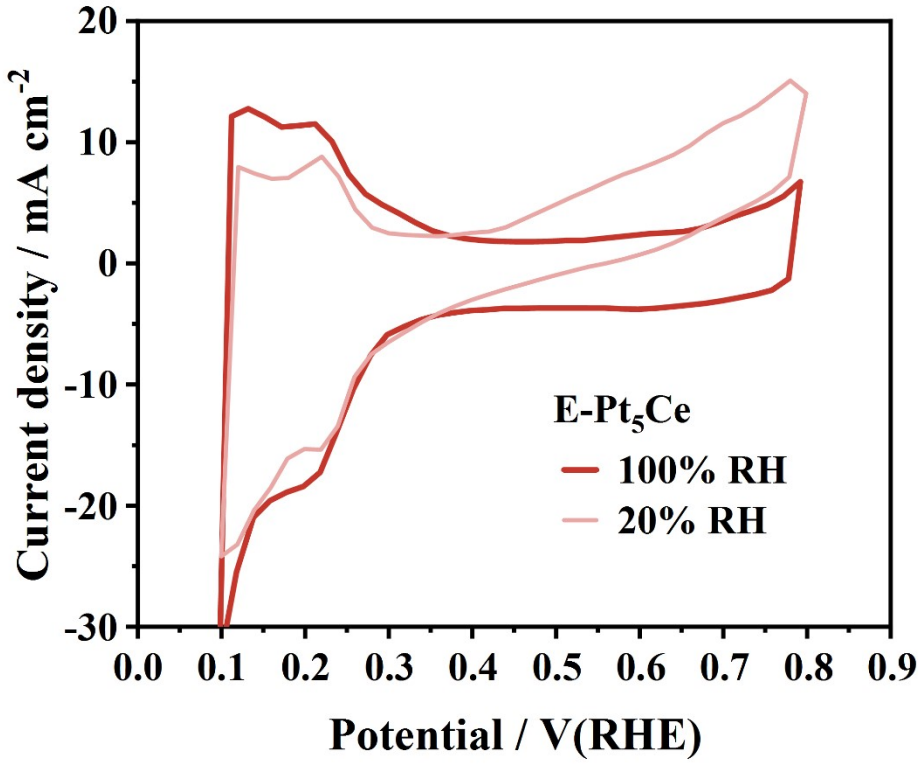

Figure S27. CV curves of E-Pt_5Ce measured at H_2/N_2 mode in 100% and 20% relative humidity.

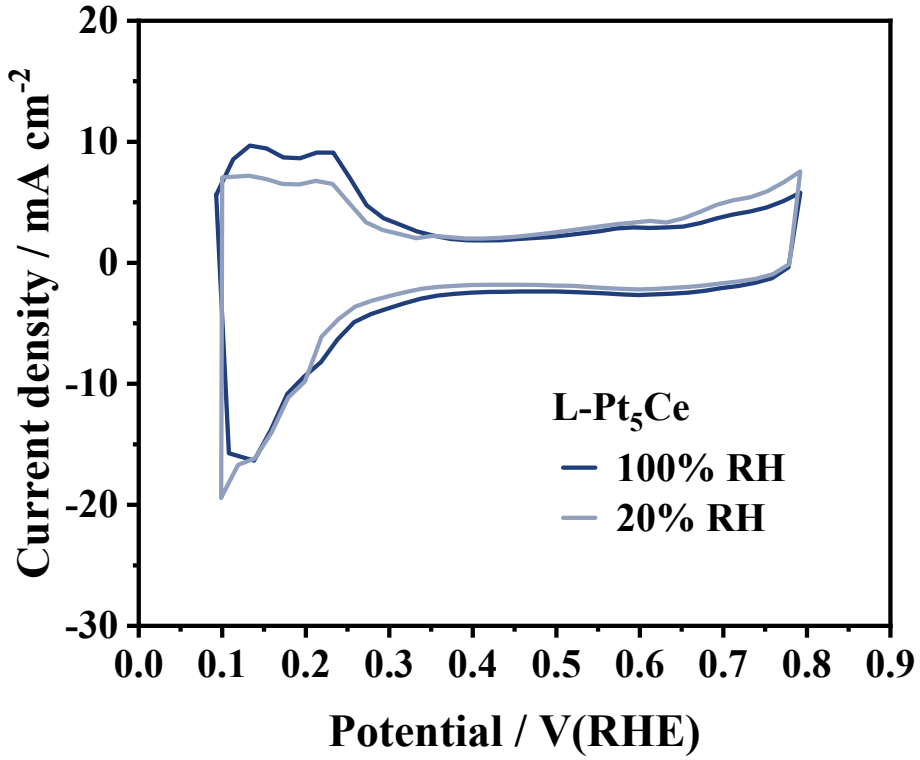

Figure S28. CV curves of L-Pt_5Ce measured at H_2/N_2 mode in 100% and 20% relative humidity.

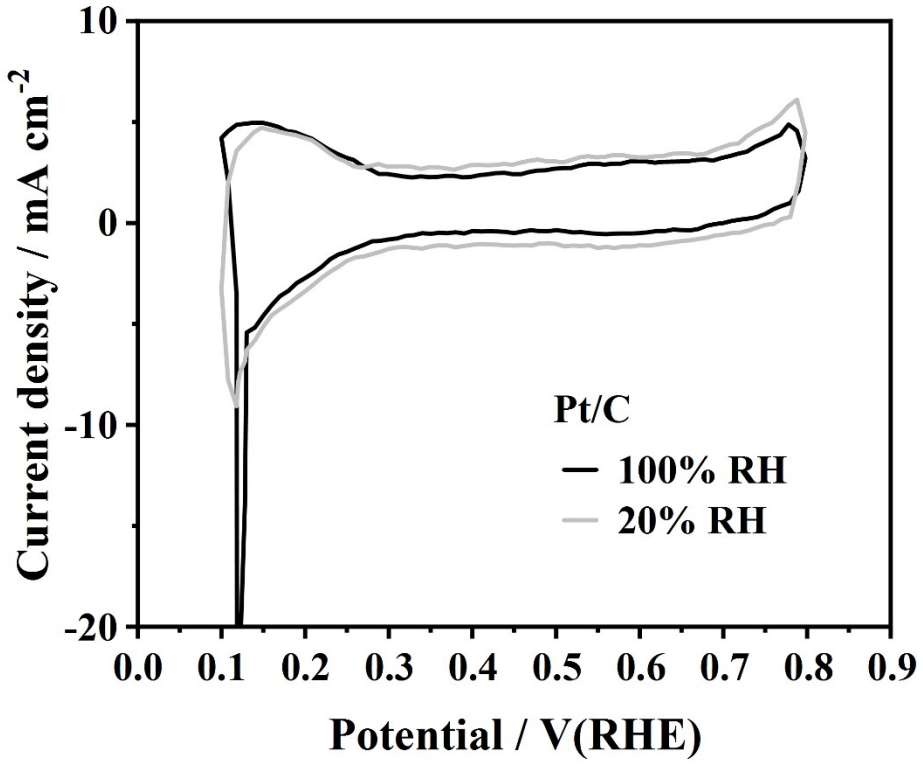

Figure S29. CV curves of Pt/Ce measured at H_2/N_2 mode in 100% and 20% relative humidity.

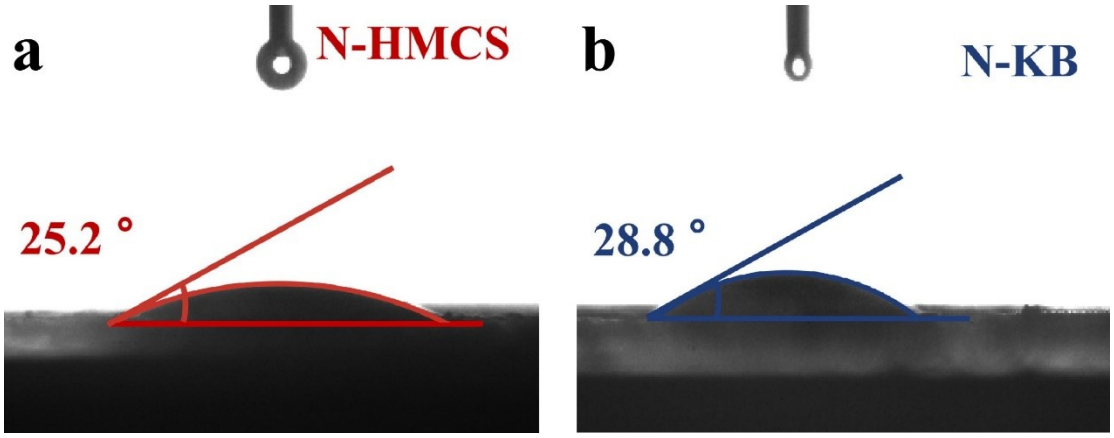

Figure S30. contact angle measurements of (a) N-HMCS. (b) N-KB.

The hydrophilicity of E-Pt_5Ce may contribute to a more uniform water uptake and distribution within the catalyst layer. This can help in maintaining the hydration state of the ionomer, which is essential for proton conductivity. Hydrophilic surfaces can promote the transport of water and dissolved oxygen towards the active sites of the catalyst. This can enhance the accessibility of reactants and potentially improve the kinetics of the ORR.

Supplementary references

[1] S. Zhu, M. Sun, B. Mei, L. Yang, Y. Chu, Z. Shi, J. Bai, X. Wang, Z. Jiang, C. Liu, B. Huang, J. Ge, W. Xing, *Natl. Sci. Rev.* **2023**, 10, nwad162.

[2] S.-L. Xu, S. Zhao, W.-J. Zeng, S. Li, M. Zuo, Y. Lin, S. Chu, P. Chen, J. Liu, H.-W. Liang, *Chem. Mater.* **2022**, 34, 10789.

[3] K. Ichihashi, S. Muratsugu, H. Matsui, K. Higashi, O. Sekizawa, T. Uruga, M. Tada, *J. Phys. Chem. C* **2020**, 124, 26925.

[4] Y. Hu, J. O. Jensen, L. N. Cleemann, B. A. Brandes, Q. Li, *J. Am. Chem. Soc.* **2020**, 142, 953.

[5] J. Fichtner, B. Garlyyev, S. Watzele, H. A. El-Sayed, J. N. Schwammlein, W. J. Li, F. M. Maillard, L. Dubau, J. Michalicka, J. M. Macak, A. Holleitner, A. S. Bandarenka, *ACS Appl. Mater. Interfaces* **2019**, 11, 5129.

[6] A. Velázquez-Palenzuela, F. Masini, A. F. Pedersen, M. Escudero-Escribano, D. Deiana, P. Malacrida, T. W. Hansen, D. Friebel, A. Nilsson, I. E. L. Stephens, I. Chorkendorff, *J. Catal.* **2015**, 328, 297.

[7] M. Escudero-Escribano, P. Malacrida, M. H. Hansen, U. G. Vej-Hansen, A. Velazquez-Palenzuela, V. Tripkovic, J. Schiotz, J. Rossmeisl, I. E. Stephens, I. Chorkendorff, *Science* **2016**, 352, 73.

[8] Y. Luo, K. Li, Y. Chen, J. Feng, L. Wang, Y. Jiang, L. Li, G. Yu, J. Feng, *Adv. Mater.* **2023**, 35, e2300624.

[9] X. Liu, J. Liang, Q. Li, Chinese *J. Catal.* **2023**, 45, 17.

[10] G. Feng, F. Ning, Y. Pan, T. Chen, J. Song, Y. Wang, R. Zou, D. Su, D. Xia, *J. Am. Chem. Soc.* **2023**, 145, 11140.

[11] Z. Qiao, C. Wang, C. Li, Y. Zeng, S. Hwang, B. Li, S. Karakalos, J. Park, A. J. Kropf, E. C. Wegener, Q. Gong, H. Xu, G. Wang, D. J. Myers, J. Xie, J. S. Spendelow, G. Wu, *Energy Environ. Sci.* **2021**, 14, 4948.

[12] C. Zhan, H. Sun, L. Lü, L. Bu, L. Li, Y. Liu, T. Yang, W. Liu, X. Huang, *Adv. Funct. Mater.* **2022**, 33.

[13] X. Liu, Z. Zhao, J. Liang, S. Li, G. Lu, C. Priest, T. Wang, J. Han, G. Wu, X. Wang, Y. Huang, Q. Li, *Angew. Chem. Int. Ed.* **2023**, 62.

[14] Z. Chen, C. Hao, B. Yan, Q. Chen, H. Feng, X. Mao, J. Cen, Z. Q. Tian, P. Tsiakaras, P. K. Shen, *Adv. Energy Mater.* **2022**, 12.

[15] J. Lin, J. Wang, Y. Wu, P. Yang, Q. Liu, M. Li, S. Du, R. Chen, L. Tao, *Chem. Asian J.* **2023**, 18, e202300137.